

Impact of Spacer Cation on the Properties of Two-Dimensional Monolayer Hybrid Halide Perovskites

Chenchen Li,^{†,‡,||} Xian Chen,^{¶,||} Tan Jin,[‡] Tianmin Wu,^{*,†} Jun Chen,^{*,‡,§} and Wei Zhuang^{*,‡,§}

[†]*College of Chemistry and Materials Science & College of Photonic and Electronic Engineering, Key Laboratory of Opto-Electronic Science and Technology for Medicine of Ministry of Education, Fujian Normal University, Fuzhou 350117, P. R. China*

[‡]*State Key Laboratory of Structural Chemistry, Fujian Institute of Research on the Structure of Matter, Chinese Academy of Sciences, Fuzhou 350002, P. R. China.*

[¶]*College of Artificial Intelligence, Yango University, Fuzhou 350015, P. R. China*

[§]*Fujian Science & Technology Innovation Laboratory for Optoelectronic Information of China, Fuzhou, Fujian 350108, P. R. China.*

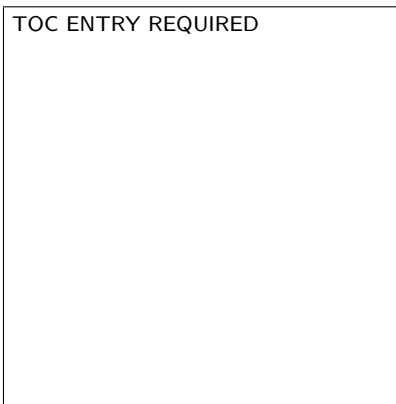
|| These authors contributed equally to this work.

E-mail: wtm@fjnu.edu.cn; chenjun@fjirms.ac.cn; wzhuang@fjirms.ac.cn

Abstract

Poor long-term stability of hybrid halide perovskites has severely inhibited their large-scale commercial applications. Recently emerging low-dimensional hybrid halide perovskites have much more enhanced long-term stability, but their wide bandgap and strong quantum well confinement severely hinder various optoelectronic applications. How to tackle these issues without sacrificing long-term stability, therefore, has been emerging as a crucial materials science concern. Based on the first principal calculations, we have investigated the impact of spacer cation on the properties of 2D monolayer hybrid halide perovskites in-depth. Our simulations reveal that strong interactions of spacer cation with each other and with MX_6^{4-} backbone not only enhance the thermostability of MX_6^{4-} backbone and protect it against water molecules, but also modulate the electronic properties via altering the crystalline structure. More importantly, the delocalized orbitals and relatively high dielectric constants of spacer cation resulting from the conjugated benzene ring weaken the quantum well confinement and potential barrier well, thus allowing the efficient electron-hole separation and photo-generated carrier out-of-plane transport. The comprehensive effect of spacer cations on the properties of 2D monolayer hybrid halide perovskites observed here, thereby, clearly demonstrates the importance of finely selected spacer cations in adopting their photophysical properties.

TOC Graphic



Introduction

As promising candidates for various optoelectronic applications, perovskite-structured materials have attracted tremendous research attention in the scientific community.¹⁻⁵ With the attractive superior virtues involving outstanding carrier mobilities, excellent optical absorption as well as low trap densities,^{6,7} the power conversion efficiency (PCEs) of organic-inorganic hybrid halide perovskites (e.g. MAPbI₃) solar cells have been boosted from 3.8% to 26.1% over the past decade.⁸ The extensive commercialization of hybrid halide perovskites is, however, largely hampered by two key challenges: poor long-term stability and severe toxicity (Pb).⁹⁻¹¹ The degradation of most hybrid halide perovskites occurs rapidly and irreversibly, due to the intrinsic low formation energy. Substituting the Pb²⁺ ion with the less toxic Sn²⁺ ion enables materials with similar optoelectronic properties to MAPbI₃, but encounter even more serious stability issues due to the easy oxidation^{12,13} of Sn²⁺ to Sn⁴⁺.

Recently emerging low-dimensional (2D) organic-inorganic hybrid halide perovskites, constructed by inserting large ammonium cation into conventional three-dimensional perovskites to form a layered structure of alternating stacked insulating organic spacer and inorganic slabs, have the promising potential to improve the long-term stability due to their intrinsic structural features.^{2,3,14-16} The hydrophobic organic spacer acts as a natural protective barrier against moisture, thus maintaining long-term stability under ambient operation conditions.^{17,18} Furthermore, the strong van der Waals interactions between organic spacers lead to an increased formation energy, and consequently higher natural lattice stability.¹⁹⁻²¹ Further reducing of the dimensionality was found to improve the perovskites' stability, with a much wider electronic bandgap away from the visible light absorption which usually results in a poor power conversion efficiency.²² On the other hand, the giant dielectric difference between the organic spacer (potential barrier) and inorganic MX₆ backbone layer (potential well) in the 2D hybrid halide perovskites structures creates a quantum well (QW), which results in the strong exciton effect, severe charge recombination, as well as the retardation of out-of-plane charge carrier transport (leading to inferior carrier mobility).^{3,23} All these

effects seriously hamper the photovoltaic performance. Furthermore, the impact of functional groups and the interactions between the spacer cations and inorganic backbone on the electronic structure and carrier transport is still not clear. How to design the composition and structure of 2D monolayer hybrid halide perovskites to narrow the electronic bandgap and promote the charge carrier transport without sacrificing long-term stability, therefore, remains a critical issue of broad interest.

Adopting the non-equilibrium Green's function theory and the density functional theory (NEGF-DFT), we herein investigated the impact of two widely applied spacer cations BA^+ ($\text{C}_4\text{H}_9\text{NH}_3^+$) and PEA^+ ($\text{C}_6\text{H}_5\text{C}_2\text{H}_4\text{NH}_3^+$) on the optoelectronic and quantum transport properties of 2D monolayer hybrid halide perovskites. Compared to BA^+ , the PEA^+ spacer cations have strong π - π stacking interactions between each other, together with strong hydrogen bonding interactions and van der Waals interactions between the PEA^+ with MX_6^{4-} backbone, which effectively narrows the electronic band gap via shortening the M-X bond length (and consequently promoting the coupling of antibonding orbitals). Three lead-free monolayer PEA-based hybrid halide perovskites are predicted to possess moderate electronic bandgaps for sunlight harvesting (1.3~1.9 eV) and reasonably good optical absorption in the visible-light range (their maximum absorption coefficient all exceeds 10^5 cm^{-1}). Among them, 2D monolayer PEA_2SnI_4 has the most promising electronic bandgap of 1.35 eV, which makes it the most attractive candidate for single-junction solar cells. Due to the relatively high dielectric constant of PEA^+ , it has a weak exciton binding effect in the selected 2D monolayer PEA_2MX_4 , which contributes to the easy photo-generated electron/hole separations. Further calculations reveal that the presence of the conjugated benzene ring in PEA^+ dramatically weakens the potential barrier of 2D monolayer PEA_2SnI_4 between the inorganic backbone and organic spacer. The potential barrier of 2D monolayer PEA_2SnI_4 -based devices (1.07 eV) is observed to be nearly 50% lower than that of 2D monolayer BA_2SnI_4 -based devices (1.56 eV). Consequently, the bias-voltage-induced current in the 2D monolayer PEA_2SnI_4 -based device is observed to be one order of magnitude higher than that of the

BA₂SnI₄-based device. More delocalized orbitals of the conjugated benzene ring in PEA⁺ indeed facilitate the connecting of quantum transport channel in the scattering region, thereby promoting the out-of-plane quantum transport of 2D monolayer PEA₂SnI₄-based device. For the stability consideration, *ab initio* molecule dynamics (AIMD) simulations show that the strong hydrogen bonding interactions and van der Waals interactions between the PEA⁺ organic spacer and the MX₆⁴⁻ backbone layer in the 2D monolayer PEA-based hybrid halide perovskites dramatically promotes their thermostability. Moreover, the hydrophobicity of the PEA⁺ spacer cation prevents the water molecule from eroding the inorganic backbone layer, which leads to good environmental stability and thus long-term stability under extreme working conditions.

Methodology

First-principles calculations for 2D monolayer hybrid halide perovskites were performed within the density-functional theory formalism (DFT), as implemented in Vienna *Ab initio* Simulation Package (VASP).^{24–26} The frozen-core projected augmented wave (PAW) method²⁷ with the generalized gradient approximation (GGA) formulated by Perdew, Burke, and Ernzerhof (PBE) as the exchange-correlation functionals²⁸ were adopted to describe the electron-core interactions. In addition, since van der Waals (vdW) interactions play a crucial role in the description of hybrid organic-inorganic halide perovskites, the effect of vdW dispersion interactions was estimated with the pairwise D3 three-body dispersion correction proposed by Grimme (DFT-D3) to describe long-range van der Waals interactions.²⁹ In all computations, the electronic wavefunctions were expanded in a plane-wave basis with an energy cutoff of 520 eV, and cell parameters and atomic positions were fully relaxed until the energy and residual forces on atoms converged to 1×10^{-6} eV and declined to 0.01 eV/Å, respectively, by applying the conjugate-gradient algorithm.^{30,31} The Brillouin zone for integrations in the reciprocal space was sampled with a Γ -centered $3 \times 3 \times 1$ *k*-point mesh. A

vacuum region of 15 Å was used to separate the slabs, in order to avoid the interaction of adjacent layers due to the periodic boundary conditions. Furthermore, finer k -point meshes were adopted for the calculations of electronic band structure, and density of states (DOS) for each configuration. To describe the electronic bandgap more consistently with the experimental results, we introduced the hybrid functional approach of Heyd, Scuseria, and Ernzerhof (HSE06)³² into our simulations for each 2D monolayer hybrid halide perovskites with 25% Hartree-Fock exchange and $\mu = 0.4 \text{ Å}^{-1}$. Additionally, the spin-orbital coupling (SOC) effect was considered in the calculation of electronic properties and optical properties. The absorption coefficient was defined as $\alpha(\omega) = \frac{\sqrt{2}e}{\hbar c} [(\varepsilon_1^2 + \varepsilon_2^2)^{\frac{1}{2}} - \varepsilon_1]^{\frac{1}{2}}$, in which ε_1 and ε_2 represent the real and imaginary part of the dielectric function, respectively. (e , \hbar and c are the electron constant, the reduced Planck constant, and the light of speed, respectively.)

AIMD simulations were performed at work temperature (350 K) by using the Nosé-Hoover method³³ to verify the thermostability of selected 2D monolayer hybrid halide perovskites. A supercell consisting of $3 \times 3 \times 1$ unit cells for selected 2D monolayer hybrid halide perovskites was constructed to perform AIMD simulations. A 5 ps NVT ensemble molecular dynamics simulation trajectory with a 0.5 fs time step was collected for selected 2D monolayer hybrid halide perovskites. Furthermore, the adsorption energy calculations were performed for the environmental stability of selected 2D monolayer hybrid halide perovskites. A supercell was constructed by stacking $3 \times 3 \times 1$ unit cells with a vacuum space larger than 20 Å along the c -axis. The absorptions of water/oxygen on the surface of 2D hybrid halide perovskites were investigated. The H₂O binding energy E_{ads} here was defined as $E_{ads} = E_{2DH_2O} - E_{2D} - E_{H_2O}$, in which E_{2DH_2O} , E_{2D} , and E_{H_2O} are the total energies of the H₂O-adsorbed 2D monolayer hybrid halide perovskites, 2D monolayer hybrid halide perovskites, and H₂O molecule, respectively.

To investigate the quantum transport properties of selected 2D monolayer hybrid halide perovskites, we constructed a vertical transport architecture device with Au electrodes acting as the source and drain contacts and 2D monolayer hybrid halide perovskites serving as

the transport channel region. Our simulations were performed by using the first-principles methods, combined with the combination of the Keldysh non-equilibrium Green's function formalism and density functional theory (NEGF-DFT),³⁴ implemented in the first principles quantum transport software package *Nanocal*.³⁴ The local density approximation (LDA)³⁵ was adopted to describe the exchange and correlation function, and atomic cores were defined by the standard norm-conserving nonlocal pseudo potentials.³⁶ A double- ζ polarized (DZP) atomic orbital basis³⁷ was used for the metal electrode (Au atom) and 2D monolayer hybrid halide perovskites to expand all physical quantities with a kinetic energy cutoff of 3000 eV. Furthermore, a k -point mesh of $7 \times 7 \times 1$ and $13 \times 13 \times 1$ was applied to sample the first Brillouin zone for integrations in the reciprocal space of scattering region (2D monolayer hybrid halide perovskites) and Au electrode, respectively. In addition, self-consistent calculations were converged until each component of the density matrix declined to 10^{-5} Hartree. For the two-probe transport junction, bias voltage was applied by setting the electrochemical potential of the left and right electrode as $\mu_L = \mu + eV_b/2$ and $\mu_R = \mu - eV_b/2$, respectively, in which μ is the common Fermi level and V_b is the applied bias voltage.

The orbital delocalization index (ODI) is introduced to identify the degree of orbital delocalization. The ODI of a particular orbital i is defined as $ODI_i = 0.01 \times \sum_A (\Theta_{A,i})^2$, where $\Theta_{A,i}$ represents the composition of atom A in orbital i . The ODI range is $(0, 100]$, the lower the ODI value, the higher the orbital delocalization. The ODI was assisted by the software Multiwfn version 3.8.³⁸ Geometry optimizations and orbital calculations of BA^+ and PEA^+ were done at B3LYP/6-311G(d,p) level of theory using Gaussian 09 software.³⁹

Results and discussion

Tuning the electronic structure of 2D monolayer PEA_2MX_4 via replacing M^{2+} and X^- ions with homogenous elements.

2D monolayer organic-inorganic hybrid halide perovskites A_2MX_4 (Figure 1a, A: Spacer cation; M: Divalent metal cation; X: Halide anion) consists of the organic spacer and separated MX_6^{4-} backbone layer. The photoelectronic properties of 12 monolayers PEA_2MX_4 perovskites are initially investigated (Figure 1a), in which M is group IV metal elements (Pb, Sn, and Ge) and X is halide elements (including F, Cl, Br, and I). Geometry optimizations using PBE-D3^{28,29} yield the lattice constants of bulk PEA_2PbI_4 : $a = 8.665 \text{ \AA}$, $b = 8.635 \text{ \AA}$, and $c = 32.546 \text{ \AA}$, which nicely agree with the experimental values of $a = 8.739 \text{ \AA}$, $b = 8.740 \text{ \AA}$, and $c = 32.093 \text{ \AA}$. The calculated in-plane lattice areas of 2D monolayer PEA_2MX_4 ($a \times b$, listed in Table S1 and Figure S1) increase with the atomic number of halide elements, due to the differences in the ionic radii and the electronegativity of halide elements ($\text{F} > \text{Cl} > \text{Br} > \text{I}$).⁴⁰

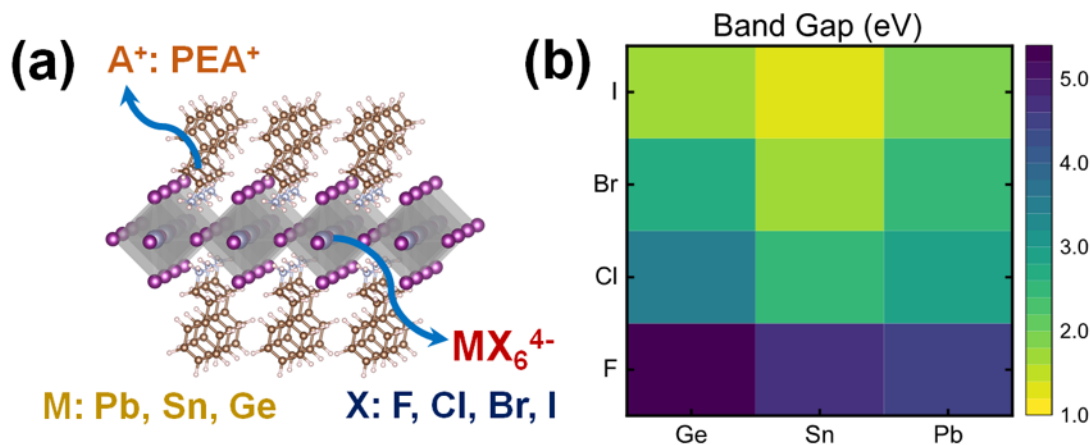


Figure 1: (a) Illustration of the monolayer PEA_2MX_4 ($\text{M} = \text{Ge}, \text{Sn}$ and Pb ; $\text{X} = \text{F}, \text{Cl}, \text{Br}$, and I). Twelve 2D monolayer hybrid halide perovskites are constructed. (b) Electronic bandgaps for 2D monolayer PEA_2MX_4 using the HSE06 + SOC level.

Since a fortuitous cancellation of errors induced by the counterbalance between GGA's natural underestimation of bandgap and the lack of spin-orbit coupling effect (SOC), PBE+vdW

functional can reproduce the experimental electronic bandgap of hybrid halide perovskites well, in which the calculated electronic bandgap (~ 2.13 eV, Figure S2) of bulk PEA_2PbI_4 is well consistent with experimental value (2.38 eV).⁴¹ The spin-orbit coupling effect (PBE+SOC), however, renders an electronic bandgap of PEA_2PbI_4 (Table S1 and Figure S2) considerably smaller than the PBE-only one, thence SOC plays an indispensable role in the electronic structure of 2D monolayer PEA_2MX_4 . Moreover, a strong correlation between PBE+SOC and HSE06+SOC level bandgap is found as a linear function with a scale factor of ~ 1.25 (Figure S3), which is consistent with the traditional wisdom.^{42,43} Bandgap values, similar to the lattice constants, correlate strongly with the atomic number of the halide elements (Figure 1b), due to the difference in the electronegativity and the ionic radii of X^- anions. The electronic band structures of PEA_2MX_4 can be further tuned by using different group IV elements for divalent cation M^{2+} . Compared to 2D monolayer PEA_2MX_4 ($\text{M}=\text{Pb}$ and Ge), the electronic bandgaps of PEA_2SnX_4 (except for PEA_2SnF_4) exhibit notably smaller values (Figure 1b), which is due to the contribution of the outmost $5p$ orbitals of Sn on the lower conduction band.

Different from the previously reported 2D monolayer hybrid halide perovskites with an electronic bandgap deviating significantly from the visible-light range required for photovoltaic applications, 4 out of 12 2D PEA-based monolayer hybrid halide perovskites that we calculated (PEA_2PbI_4 : 1.84 eV, $\text{PEA}_2\text{SnBr}_4$: 1.79 eV, PEA_2SnI_4 : 1.35 eV, and PEA_2GeI_4 : 1.75 eV) possess the promising bandgaps for high photovoltaic performance. Electronic band structures of these four materials calculated using PBE, PBE+SOC, and HSE06+SOC functionals are presented in Figures S4 to S7, respectively. Among them, high-toxic lead content in 2D monolayer PEA_2PbI_4 leads to both environmental and health issues,^{6,11} therefore, we don't consider it in the following discussions. The orbital projected electronic band structures of the remaining three 2D monolayers with the HSE06+SOC functional are demonstrated in Figures 2a and S8, respectively. Interestingly, the electronic bandgap of 2D monolayer PEA_2SnI_4 is 1.35 eV, which agrees very nicely with the required optimum bandgap value

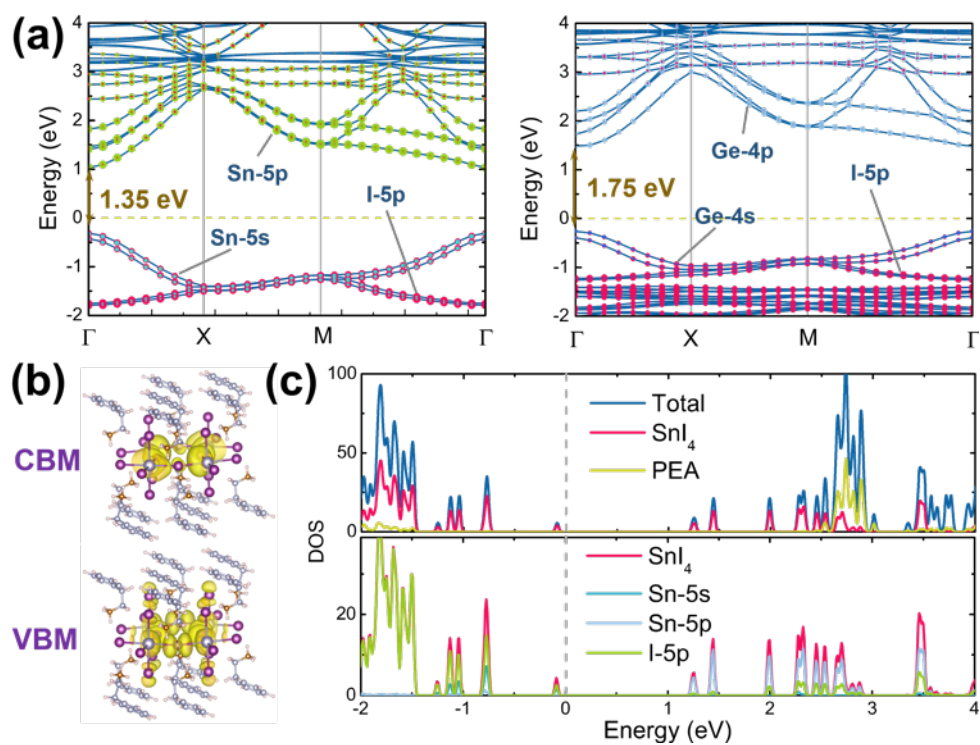


Figure 2: (a) Orbital-projected electronic band structure of 2D monolayer PEA₂SnI₄ and PEA₂GeI₄. The red, cyan, and green color corresponds to Sn-5p states, Sn-5s states, and I-5p states, respectively. (b) Decomposed charge densities of VBM (Sn-5s and I-5p orbital overlap) and CBM (Sn-5p orbitals) (isovalue = 0.001 eÅ⁻³). (c) Projected density of states for 2D monolayer PEA₂SnI₄.

(1.34 eV) according to the Shockley-Queisser-efficiency limit for single-junction semiconductor solar cells.⁴⁴

For 2D monolayer PEA_2SnI_4 , the conduction band stems mostly from the $5p$ orbital of Sn, while the hybrid state between Sn- $5s$ and I- $5p$ orbitals mainly contributes to the valence band (Figure 2a). Similarly, the valence band and conduction band of $\text{PEA}_2\text{SnBr}_4$ (PEA_2GeI_4) are mainly derived from the $5p$ orbital of Sn ($4p$ orbital of Ge) and a hybrid state between Sn- $5s$ and Br- $4p$ orbitals (Ge- $4s$ and I- $5p$ orbitals), respectively. The decomposed charge densities (Figures 2b and S9) correspond to the valence band maximum (VBM) and conduction band minimum (CBM) locate on the inorganic MX_6^{4-} backbone layer. The calculated electronic band structure, therefore, shows that VBM and CBM are primarily contributed from metal cation and halogen anions, namely, the MX_6^{4-} inorganic framework. The projected density of states (PDOS, Figures 2c, S10, and S11) also indicates that the electronic band structure is mainly dominated by the inorganic MX_6^{4-} backbone layers. It is therefore effective to tune the electronic structures by replacing either divalent cation M^{2+} or halide anion X^- .

The spacer cation impact on the electronic band structure.

Spacer cations make much less contribution to the electronic band structure compared to the anionic backbone layers, but they have an indirect impact on the electronic band structure via affecting the MX_6^{4-} octahedra. Strong π - π stacking interactions between the PEA^+ spacer cations, together with strong hydrogen bonding interactions and van der Waals interactions between the PEA^+ spacer cations and the MX_6^{4-} backbone makes the average Sn-I bond length of 2D monolayer PEA_2SnI_4 (2.156 Å, Figure S12) shorter than those of 2D monolayer BA_2SnI_4 (2.173 Å, Figure S12). The coupling between Sn- $5s$ and I- $5p$ antibonding orbitals is therefore enhanced, and their electron wavefunctions are much more significantly overlapped. This results in the narrowing of the electronic bandgap (1.35 eV and 1.56 eV for 2D monolayer PEA_2SnI_4 and BA_2SnI_4 , respectively, Figure S13).

The effective masses of electrons (m_e^*) and holes (m_h^*) in monolayer 2D PEA_2SnI_4 ,

Table 1: Selected 2D monolayer hybrid perovskites with relevant statistics

	m_e^* (m_e)	m_h^* (m_e)	ΔE_{ads} (eV)	E_b (meV)	a_0 (Å)
PEA ₂ GeI ₄	0.33	0.16	-0.28	91.51	19.47
PEA ₂ SnBr ₄	0.22	0.23	-0.30	47.47	26.73
PEA ₂ SnI ₄	0.20	0.18	-0.26	91.51	25.71
BA ₂ SnI ₄ ⁴⁵	0.29	0.37	/	267	9.21

PEA₂SnBr₄, and PEA₂GeI₄ are presented in Table 1, $m^* = \hbar^2(\partial^2 E/\partial k^2)$, \hbar , and k are the reduced Plank constant and the magnitude of wavevector in the momentum space, respectively. These effective masses of electrons/holes are close to the effective masses of electrons/holes in the representative MAPbI₃ (0.298/0.275 m_e),⁴⁶ which indicates that the investigated atomically thin 2D hybrid halide perovskites possess excellent charge carrier mobility and transport properties for various optoelectronic applications. Compared to BA⁺ spacer cation, as listed in Table 1, PEA⁺ not only reduces the electronic bandgap of PEA₂SnI₄ via promoting the coupling between Sn-5s and I-5p antibonding orbitals but also enhance the band dispersion of CBM and VBM, thereby lead to a slight reduction of effective masses for electron (m_e^*) and hole (m_h^*) and potentially high carrier mobility. The calculated effective masses of electron/hole in bulk PEA₂SnI₄, PEA₂SnBr₄, and PEA₂GeI₄ (Table S2) are slightly heavier than the corresponding atomically thin 2D hybrid halide perovskites, which suggests that reducing the material dimension may promote the charge carrier mobility and transport properties.

The computed optical absorption spectra of three 2D monolayer PEA₂MX₄ (Figure 2a) are compared with those of MAPbI₃. 2D monolayer PEA₂SnI₄, PEA₂SnBr₄, and PEA₂GeI₄ all exhibit a low absorption in the visible-light range from 1.59 to 3.26 eV. 2D monolayer PEA₂SnBr₄ and PEA₂GeI₄, have similar absorption coefficients in the visible-light range due to their closed electronic bandgap values, while 2D monolayer PEA₂SnI₄ shows higher absorption in near-infrared range due to a narrow bandgap. Despite that, all selected 2D monolayer PEA-based hybrid halide perovskites show reasonably good absorption in the visible-light range (their maximum absorption coefficient all exceed $1 \times 10^5 \text{ cm}^{-1}$), indicating

that most output of Sun's total irradiance spectrum can be absorbed. These desirable optical absorption properties render 2D monolayer PEA_2SnI_4 , $\text{PEA}_2\text{SnBr}_4$, and PEA_2GeI_4 promising sunlight-harvesting materials with potentially high efficiency.

Thermal and environmental stabilities of 2D monolayer PEA_2SnI_4 , $\text{PEA}_2\text{SnBr}_4$, and PEA_2GeI_4 .

Thermal and environmental stabilities are the key issues for the practical application of hybrid halide perovskites as photovoltaic materials. Most of the reported hybrid halide perovskites with high power conversion efficiency (PCE) suffer from structural degradation at the working conditions, with their degeneration mechanism remaining largely unclear. It's widely believed that moist (H_2O) acts as the reactive source for the collapse of the inorganic framework. We therefore evaluated the environmental stabilities of 2D monolayer PEA_2SnI_4 , $\text{PEA}_2\text{SnBr}_4$, and PEA_2GeI_4 by calculating the adsorption energies of water molecules on their surfaces. The calculated adsorption energies are listed in Table 1, and the corresponding optimized configurations of H_2O molecules adsorbed on the surface of each compound are illustrated in Figure 3b, respectively. Compared with MAPbI_3 (-0.48 eV), 2D monolayer PEA_2SnI_4 (-0.26 eV), $\text{PEA}_2\text{SnBr}_4$ (-0.3 eV), and PEA_2GeI_4 (-0.28 eV) exhibit smaller adsorption energies of H_2O on the surfaces, which suggest a better moisture resistance. Further microstructural analysis reveals that (Figure 3b) there is no hydrogen bonding interaction between the benzene ring in PEA^+ and the water molecule. Moreover, the weak hygroscopicity of PEA^+ leads to the separation of the water molecule and the inorganic framework, which inhibits the water-induced distortions of the inorganic framework at the surface. The increment in the energy barrier of the H_2O penetration process thereby prevents the hydration degradation of PEA-based 2D monolayer hybrid halide perovskites in practical applications.

We further evaluated the thermodynamic stabilities of 2D monolayer $\text{PEA}_2\text{SnBr}_4$ and PEA_2SnI_4 using *ab initio* molecular dynamics (AIMD) simulations at a working temperature

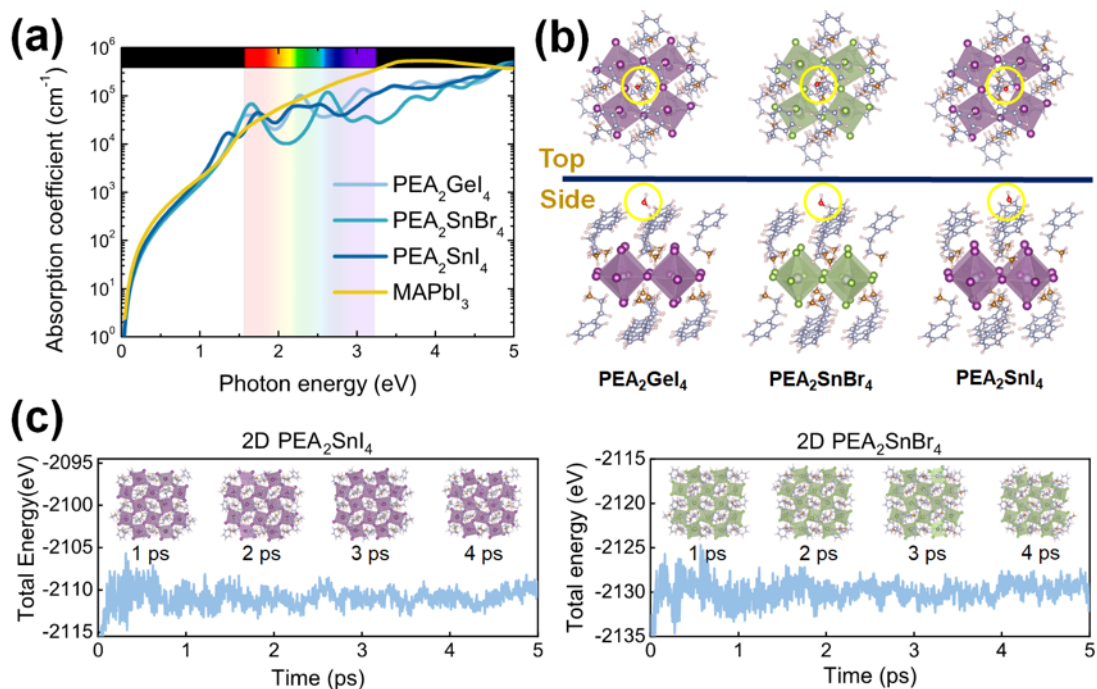


Figure 3: (a) Linear absorption spectra of three PEA-based 2D hybrid halide perovskites, including 2D monolayer PEA₂GeI₄, PEA₂SnBr₄ and PEA₂SnI₄, compared with the optical absorption spectra of MAPbI₃. (b) Top and side views of configurations for PEA-based 2D hybrid halide perovskites with one H₂O adsorbed on the surface after optimization. (c) Total energy during 5 ps AIMD simulations for 2D monolayer (left) PEA₂SnI₄ and (right) PEA₂SnBr₄, respectively.

of 350 K. Total energies of both systems (Figure 3c) fluctuate within a narrow energy range, indicating the structural integrity with no phase transitions even at the extreme operating temperature. Snapshots of 2D monolayer $\text{PEA}_2\text{SnBr}_4$ and PEA_2SnI_4 (taken every picosecond, Figure 3c) show that their inorganic framework (e. g. the ordered configuration with networks of corner-sharing octahedrons) are well sustained during the simulations. The differences between the inorganic perovskite framework of the two compounds are also markedly reflected in the simulated XRD diffraction pattern. Consistent diffraction peaks in the XRD diffraction patterns at different moments along the trajectory (Figures S14 and S15) further suggest that the perovskite framework is stable at high operation temperature (350 K).

The radial distribution functions (RDF) and root mean square distances (RMSD) of the inorganic octahedral framework (MX_6^{4-}) are calculated based on the simulation trajectories of $\text{PEA}_2\text{SnBr}_4$ and PEA_2SnI_4 . The RDF between two components a and b ($g_{ab}(r)$) are defined as

$$g_{ab}(r) = (N_a N_b)^{-1} \sum_{i=1}^{N_a} \sum_{j=1}^{N_b} \langle \delta(|r_i - r_j| - r) \rangle \quad (1)$$

where N_a , N_b are the number of components a and b , respectively. The calculated radial distribution functions of the Sn-Br and Sn-I pairs in 2D monolayer $\text{PEA}_2\text{SnBr}_4$ and PEA_2SnI_4 are illustrated in Figures 4a and S16, respectively. Strong first peak at $\sim 3.0 \text{ \AA}$ and $\sim 3.2 \text{ \AA}$ are consistent with the corresponding bond lengths of Sn-Br and Sn-I in the lattice structure of 2D monolayer $\text{PEA}_2\text{SnBr}_4$ and PEA_2SnI_4 , respectively, indicating that their inorganic octahedral frameworks do not suffer degeneration at high operation temperature (350 K). Broadening of the first peak and the second peak of Sn-Br and Sn-I RDFs clearly show the thermo-distortion of the inorganic octahedral framework. The RMSD as a function of evolution time is calculated as

$$\rho(t) = \sqrt{\frac{1}{N} \sum_{i=1}^N w_i (x_i(t) - x_i^{\text{ref}})^2} \quad (2)$$

in which N is the number of selected atoms, $x_i(t)$ is the coordinates of atom i at time t , x_i^{ref} is the coordinates of reference atoms, and w_i is the weight whose default value is 1. Time-dependent RMSD (Figure 4b) for halide atoms (Br and I) in 2D monolayer $\text{PEA}_2\text{SnBr}_4$ and PEA_2SnI_4 oscillate within a narrow range compared to the DFT-optimized structure. The selected 2D monolayer hybrid halide perovskites can therefore maintain their structural integrity at high operation temperatures. Besides RDF and RMSD of the inorganic octahedral framework (MX_6^{4-}), the dihedral angles of PEA^+ are also calculated to reveal the interactions between the PEA^+ groups and the inorganic halide frameworks $\text{SnBr}_6^{4-}/\text{SnI}_6^{4-}$. The dihedral and torsion angle of PEA^+ in the current study (Figure 4c) is defined by N atoms and benzene rings and by the angle between the plane of the benzene ring and the plane containing N-C-C, respectively. Time-dependent dihedral and torsion angle for PEA^+ in both 2D monolayer $\text{PEA}_2\text{SnBr}_4$ and PEA_2SnI_4 oscillate within a narrow range (Figures 4b and S17), in which the dihedral and angle of PEA^+ in 2D monolayer PEA_2SnI_4 oscillates from $\sim 120^\circ$ to $\sim 135^\circ$ and from $\sim 95^\circ$ to $\sim 112^\circ$, respectively. The shape of PEA^+ spacer cations therefore does not change or undergo structural deformation at the extreme operating conditions of 350 K.

Time-dependent average distances for N (PEA^+)-Sn/I (SnI_6^{4-} backbone) and N (PEA^+)-Sn/Br (SnBr_6^{4-} backbone) oscillate within a narrow range (~ 4.38 Å and ~ 3.45 Å for 2D monolayer PEA_2SnI_4 and ~ 4.08 Å and ~ 3.09 Å for 2D monolayer $\text{PEA}_2\text{SnBr}_4$, respectively (Figures 4d and S18). PEA^+ in both 2D monolayer $\text{PEA}_2\text{SnBr}_4$ and PEA_2SnI_4 therefore does not drift away from the framework at 350 K. Hydrogen bonds form between the spacer cation PEA^+ and the inorganic $\text{SnBr}_6^{4-}/\text{SnI}_6^{4-}$ inorganic backbone (N-H \cdots I/Br, Figure 4f). A PEA^+ spacer cation can form three hydrogen bonds in the Sn-I/Br cage ($\text{HB}_{\text{N-H}\cdots\text{I/Br}} < 3$ Å) for both 2D monolayers $\text{PEA}_2\text{SnBr}_4$ and PEA_2SnI_4 . The time-dependent average distance for H (NH_3^+ group in PEA^+)-Br/I ($\text{SnBr}_6^{4-}/\text{SnI}_6^{4-}$ backbone) oscillates in the range of 2.18~2.4 Å for 2D monolayer $\text{PEA}_2\text{SnBr}_4$ / PEA_2SnI_4 (Figures 4f and S19), which indicates the strong hydrogen bonding interactions between PEA^+ and MX_6^{4-} backbone layer. These hydrogen

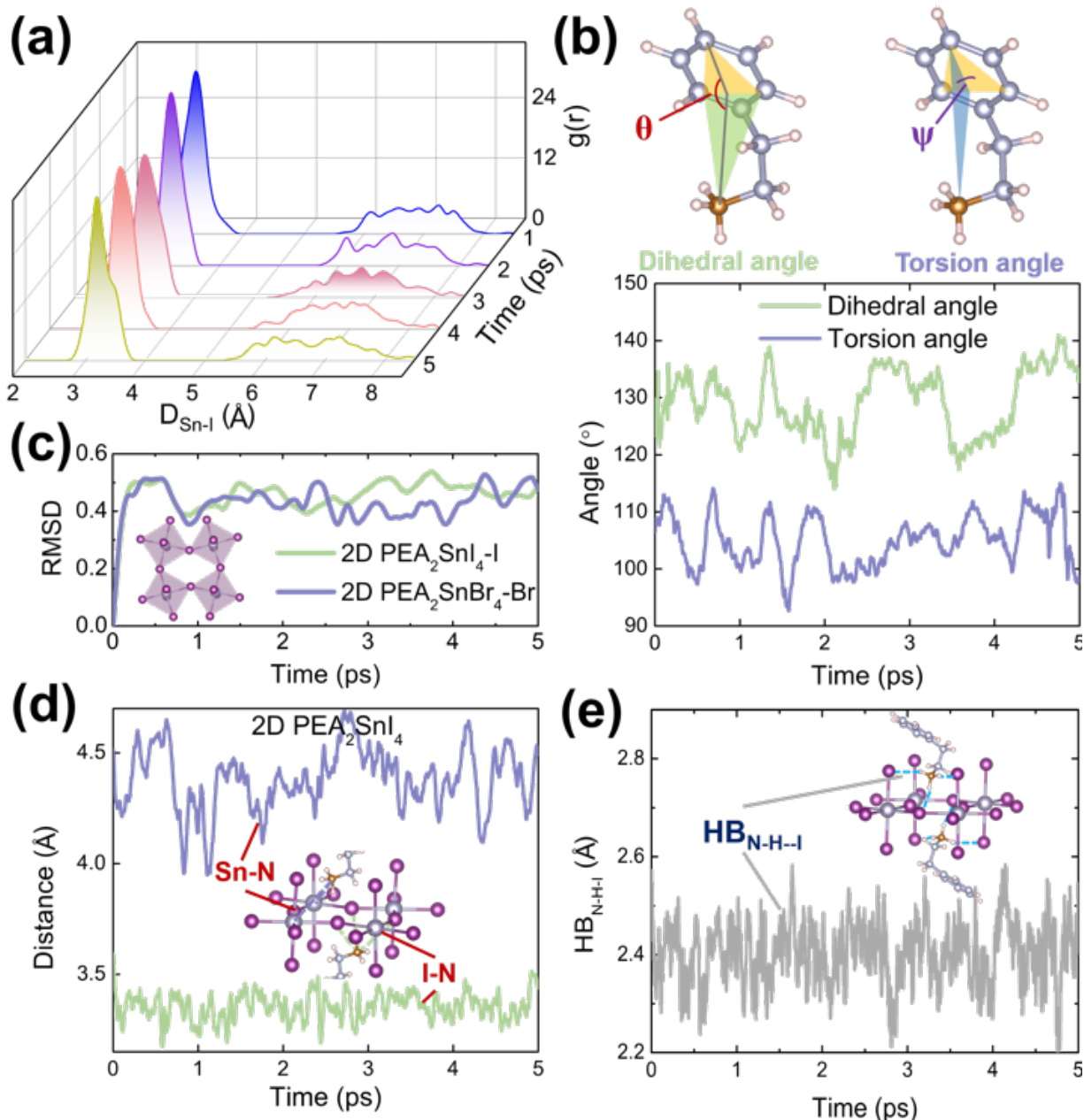


Figure 4: (a) Time-dependent radial distribution function of Sn-I in 2D monolayer PEA_2SnI_4 at 350 K. (b) Dihedral angle (left) and torsion angle (right) of PEA^+ spacer cation in 2D monolayer PEA_2SnI_4 during 5 ps AIMD simulations at 350 K. (c) Root mean square deviation of I and Br compared with their initial optimized positions in 2D monolayer $\text{PEA}_2\text{SnBr}_4$ and PEA_2SnI_4 , respectively. (d) Distance between Sn-N and I-N in 2D monolayer PEA_2SnI_4 during 5 ps AIMD simulations. (e) Time-dependent hydrogen bond length $\text{HB}_{\text{N-H}\dots\text{I}}$ in 2D monolayer PEA_2SnI_4 .

bonding interactions, together with the van der Waals interactions between the spacer cation and the inorganic framework, significantly enhance the thermostability of 2D monolayer hybrid halide perovskites at extreme operating conditions. 2D monolayer $\text{PEA}_2\text{SnBr}_4$ and PEA_2SnI_4 , thereby, maintain their structures at extreme operating conditions (e. g. the ambient atmosphere and high temperature), without suffering from structural deformation or decomposition, and potentially address short-term stability as a primary concern of the community.

Quantum well confinement and the out-of-plane carrier transport in 2D monolayer BA_2SnI_4 and PEA_2SnI_4 .

Although 2D monolayer hybrid halide perovskites potentially possess superior long-term stability under ambient environments, the quantum well confinement originating from the arrangement of the large-size spacer cation (act as a potential barrier) and the inorganic MX_6^{4-} slab (as a potential well) substantially increases the exciton binding energy and blocks the out-of-plane carrier transport. The exciton binding energy and in-plane Wannier-Mott exciton radii are roughly estimated based on the effective mass theory ($E_b = \mu e^4 / 2\hbar^2 \varepsilon^2$, $a_0 = \hbar^2 \varepsilon / \mu e^2$), where ε is the dielectric constant and $\mu = (m_e^* \times m_h^*) / (m_e^* + m_h^*)$ is the reduced effective mass and e is the charge of an electron.^{47,48} The calculated exciton binding energy (Table 1) of all selected PEA-based 2D monolayer hybrid halide perovskites are much larger with respect to that of MAPbI_3 (~ 15 meV),⁴⁹ which undoubtedly inhibit the photon-induced electron-hole separations. Compared to 2D monolayer BA_2MX_4 , the selected 2D monolayer PEA_2MX_4 possess smaller exciton binding energy and larger exciton radius. The small exciton binding energy of 2D monolayer PEA_2MX_4 should stem from the relatively high dielectric constant of PEA^+ spacer cation,^{50,51} as evaluated by the dielectric constant model. The larger dielectric constant of PEA^+ further indicates the importance of functional group (e. g. the benzene ring) in weakening the quantum well confinement effect and reducing the exciton binding energy for electron-hole separations.

Besides the inhibition effect of the quantum well structure on the electron-hole separation, the insulating effect of the spacer cation also hinders the out-of-plane charge carrier transports. Based on the Keldysh non-equilibrium Green's function formalism and density functional theory (NEGF-DFT), the out-of-plane quantum transport properties of 2D monolayer PEA₂SnI₄⁻ and BA₂SnI₄-based devices are investigated by constructing vertical transport architecture devices containing the Au electrodes and the 2D monolayer hybrid halide perovskites acting as the scattering region (Figures 5a and S20), as we previously constructed all-metallic vertical tunneling architecture.⁵² The calculated potential energy distribution of 2D monolayer PEA₂SnI₄⁻ and BA₂SnI₄-based vertical transport architecture along *ab*-plane are illustrated in Figure S21, respectively. The out-of-plane tunneling currents of 2D monolayer PEA₂SnI₄⁻ and BA₂SnI₄-based devices are calculated by integrating the transmission coefficient over the bias window:⁵³

$$I(V_b) = \frac{2e}{h} \int_{\mu_R}^{\mu_L} T(E, V_b) [f(E - \mu_L) - f(E - \mu_R)] dE \quad (3)$$

Where $f(E - \mu_L/\mu_R) = 1 / \left(e^{\frac{E - \mu_L/\mu_R}{k_B T}} + 1 \right)$ are the Fermi-Dirac distribution functions of an electron. The transmission function, $T(E, V_b)$, were calculated using the Landauer-Büttiker formula:⁵¹

$$T(E, V_b) = Tr [\Gamma_L(E)G^R(E)\Gamma_R(E)G^A(E)] \quad (4)$$

Where $G^R(E)$ and $G^A(E)$ represent the retarded and advanced Green's functions of the scattering region. $\Gamma_L(E)$ and $\Gamma_R(E)$ are the linewidth functions of the left and right Au electrodes describing the coupling between electrodes and the scattering region. V_b , μ_L , and μ_R are the bias voltage and the electrochemical potential of the left/right Au electrodes, respectively.

The potential barrier of the 2D monolayer BA₂SnI₄-based device is nearly 50% larger than that of the 2D monolayer PEA₂SnI₄-based device (1.56 eV vs. 1.07 eV, Figure 5b). The same inorganic backbone layer (SnI₆⁴⁻) leads to similar contributions to the potential

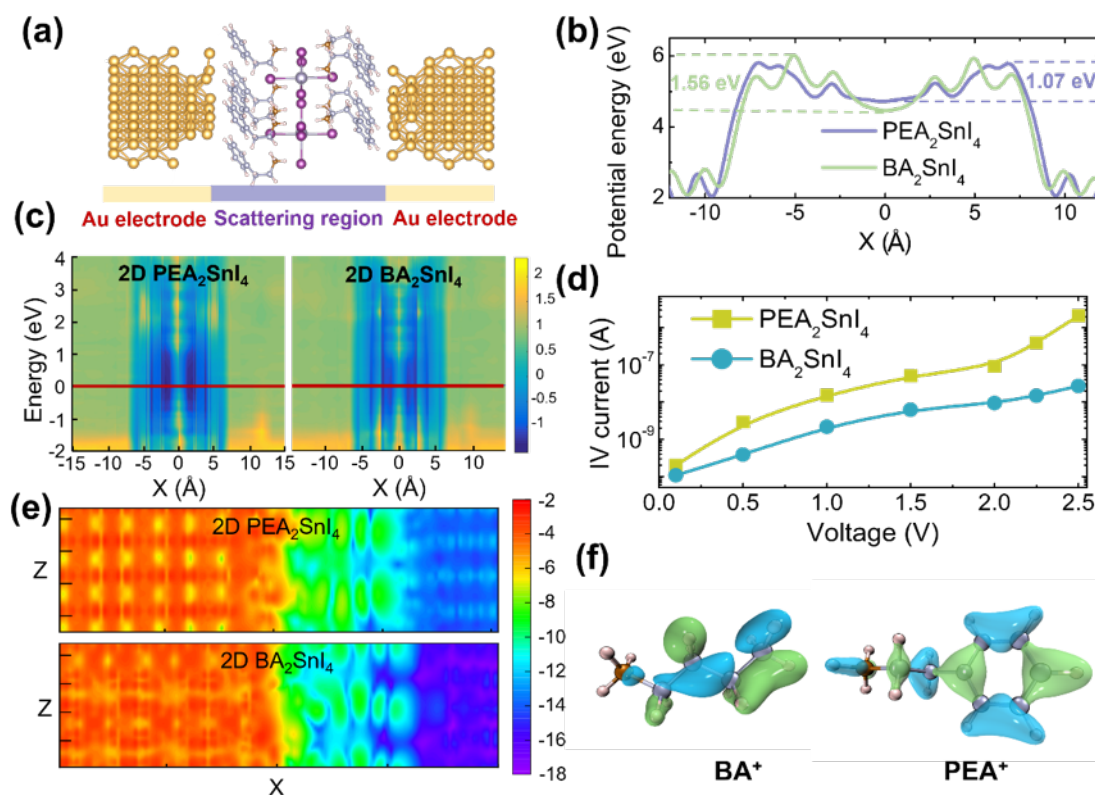


Figure 5: (a) Side view of the atomic structure of the vertical transport architecture. (b) The average potential energy of 2D monolayer PEA_2SnI_4 - (purple) and BA_2SnI_4 -based devices (green) along the transport direction (x -axis). (c) PDOS for 2D monolayer PEA_2SnI_4 - and BA_2SnI_4 -based devices by different colors along the x -axis transport direction. The red line represents the Fermi energy level. (d) Current-Voltage (I-V) curves of 2D monolayer PEA_2SnI_4 - and BA_2SnI_4 -based devices. (e) Realspace scattering states of 2D monolayer PEA_2SnI_4 - and BA_2SnI_4 -based devices under the bias voltage of 1.4 V and at the gamma point with the same color bar. (f) Low ODI molecular orbital diagrams of BA^+ and PEA^+ along with the ODI.

well. Thence, the significant difference in the potential barrier should mainly stem from the different spacer cations. Considering the similar thickness of the organic spacer (similar length of PEA⁺ and BA⁺), the functional group should play a crucial role in the out-of-plane potential barrier and carrier transport of 2D monolayer hybrid halide perovskites. Realspace PDOS for 2D monolayer PEA₂SnI₄- and BA₂SnI₄-based devices (Figure 5c) further confirms that the existence of significant potential barriers (dark blue region) induced by 2D monolayer hybrid halide perovskites (from -8 to 8 Å, semiconductor scattering region).

The low potential barrier investigated in 2D monolayer PEA₂SnI₄-based device, therefore, favors the out-of-plane transport of photo-generated charge carrier and weakens the charge recombination. Current-voltage (I-V) curves (Figure 5d) show that the bias voltage-driven current of 2D monolayer PEA₂SnI₄-based device is almost one order of magnitude larger than those of 2D monolayer BA₂SnI₄-based one. The lower out-of-plane potential barrier arising from the PEA⁺ spacer cation (the conjugated benzene ring) substantially facilitates the out-of-plane carrier transports. For the 2D monolayer PEA₂SnI₄-based device, a proper current I_{ON}/I_{OFF} ratio (3 orders of magnitude) can be achieved, indicates that 2D monolayer PEA₂SnI₄ is also a promising candidate for the applications in field-effect transistors (FETs). Real-space scattering states of 2D monolayer BA₂SnI₄- and PEA₂SnI₄-based devices under the bias voltage of 1.4 V and at the gamma high symmetry point are illustrated in Figure 5e. Along the out-of-plane transport direction, the 2D monolayer PEA₂SnI₄-based device has much more available transport channels than the 2D monolayer BA₂SnI₄-based one. PEA⁺ spacer cation in the scattering region, therefore, contributes more to the quantum transport than the BA⁺ spacer cation. Our calculations reveal that the conjugation of the benzene ring in the PEA⁺ spacer cation makes the orbital more delocalization, as intuitively reflected in the lower ODI (Figure S22). The average ODIs of BA⁺ and PEA⁺ spacer cation on the occupied molecular orbital are evaluated to be 55.11 and 31.33, respectively. The low ODI molecular orbital diagrams of BA⁺ and PEA⁺ are shown in Figure 5f. Benefits to a relatively wider spatial delocalization stem from the benzene ring, PEA⁺ spacer cation

promotes a significant increment in the out-of-plane quantum transport.

Conclusions

To summarize, the current study reveals that the spacer cations, especially their functional group, play an important role in the optoelectronic properties, thermostability, and photo-generated carrier transport in 2D monolayer hybrid halide perovskites. Compared to the BA^+ spacer cation, the strong π - π stacking interactions between each other together with strong hydrogen bonding interactions and van der Waals interactions between the PEA^+ with MX_6^{4-} backbone effectively narrow the electronic bandgap via shortening the M-X bond length to promote the coupling of antibonding orbitals. In particular, 2D monolayer PEA_2SnI_4 is simulated to possess a proper electronic bandgap (~ 1.35 eV, well consistent with the optimum value according to the Shockley-Queisser limit) and reasonably good optical absorption in the visible-light range for photovoltaic applications. In addition, the hydrophobicity of PEA^+ can well prevent the attack of water molecules on the inorganic MX_6^{4-} backbone, and the strong hydrogen bonding interactions and van der Waals interactions between the PEA^+ spacer cations with MX_6^{4-} backbone let 2D monolayer PEA_2MX_4 exhibit excellent thermal stability under the extreme operating conditions. Moreover, the delocalized orbitals of the conjugated benzene ring in PEA^+ and its relatively high dielectric constants were found to weaken the quantum well confinement and potential barrier well, thus allowing the effective electron-hole separations and photogenerated carrier out-of-plane transport. The functional group, such as the conjugated benzene ring, thence not only plays a critical role in the modulation of optoelectronic properties of 2D monolayer hybrid halide perovskites (e. g. the electronic bandgap and carrier mobility) but also in the long-term stability and photogenerated carrier out-of-plane transports.

Acknowledgement

This work was financially supported by the National Natural Science Foundation of China (Grant Nos. 22103012, 22173104) and the Fujian Science & Technology Innovation Laboratory for Optoelectronic Information of China (Grant No. 2021ZR109). We gratefully acknowledge HZWTECH for providing computation facilities.

References

- (1) Huang, J.; Yuan, Y.; Shao, Y.; Yan, Y. Understanding the physical properties of hybrid perovskites for photovoltaic applications. *Nat. Rev. Mater.* **2017**, *2*.
- (2) Grancini, G.; Nazeeruddin, M. K. Dimensional tailoring of hybrid perovskites for photovoltaics. *Nat. Rev. Mater.* **2019**, *4*, 4–22.
- (3) Blancon, J. C.; Even, J.; Stoumpos, C. C.; Kanatzidis, M. G.; Mohite, A. D. Semiconductor physics of organic-inorganic 2D halide perovskites. *Nat. Nanotechnol.* **2020**, *15*, 969–985.
- (4) Wu, T.; Wang, J. Global discovery of stable and non-toxic hybrid organic-inorganic perovskites for photovoltaic systems by combining machine learning method with first principle calculations. *Nano Energy* **2019**, *66*, 104070.
- (5) Lu, S.; Zhou, Q.; Ouyang, Y.; Guo, Y.; Li, Q.; Wang, J. Accelerated discovery of stable lead-free hybrid organic-inorganic perovskites via machine learning. *Nat. Commun.* **2018**, *9*, 3405.
- (6) Wang, R.; Wang, J.; Tan, S.; Duan, Y.; Wang, Z.-K.; Yang, Y. Opportunities and Challenges of Lead-Free Perovskite Optoelectronic Devices. *Trends Chem.* **2019**, *1*, 368–379.

- (7) Zhou, N.; Zhou, H. Spacer Organic Cation Engineering for Quasi-2D Metal Halide Perovskites and the Optoelectronic Application. *Small Struct.* **2022**, *3*, 2100232.
- (8) National Renewable Energy Laboratory of the United States of America (NREL) National Center for Photovoltaics, Best Research-Cell Efficiencies chart. <https://www.nrel.gov/pv/assets/pdfs/best-research-cell-efficiencies.20200925.pdf>, accessed Aug. 7 2023.
- (9) Li, D.; Shi, J.; Xu, Y.; Luo, Y.; Wu, H.; Meng, Q. Inorganic–organic halide perovskites for new photovoltaic technology. *Natl. Sci. Rev.* **2018**, *5*, 559–576.
- (10) Zhao, Y.; Zhu, K. Organic-inorganic hybrid lead halide perovskites for optoelectronic and electronic applications. *Chem. Soc. Rev.* **2016**, *45*, 655–89.
- (11) Ju, M.-G.; Chen, M.; Zhou, Y.; Dai, J.; Ma, L.; Padture, N. P.; Zeng, X. C. Toward Eco-friendly and Stable Perovskite Materials for Photovoltaics. *Joule* **2018**, *2*, 1231–1241.
- (12) Kim, B.; Seok, S. I. Molecular aspects of organic cations affecting the humidity stability of perovskites. *Energy Environ. Sci.* **2020**, *13*, 805–820.
- (13) Saparov, B.; Mitzi, D. B. Organic-Inorganic Perovskites: Structural Versatility for Functional Materials Design. *Chem. Rev.* **2016**, *116*, 4558–96.
- (14) Wu, G.; Liang, R.; Zhang, Z.; Ge, M.; Xing, G.; Sun, G. 2D Hybrid Halide Perovskites: Structure, Properties, and Applications in Solar Cells. *Small* **2021**, *17*, e2103514.
- (15) Ratte, J.; Macintosh, M. F.; DiLoreto, L.; Liu, J.; Mihalyi-Koch, W.; Hautzinger, M. P.; Guzei, I. A.; Dong, Z.; Jin, S.; Song, Y. Spacer-Dependent and Pressure-Tuned Structures and Optoelectronic Properties of 2D Hybrid Halide Perovskites. *J. Phys. Chem. Lett.* **2023**, *14*, 403–412.

- (16) Zhang, J.; Song, X.; Wang, L.; Huang, W. Ultrathin two-dimensional hybrid perovskites toward flexible electronics and optoelectronics. *Natl. Sci. Rev.* **2022**, *9*, nwab129.
- (17) Lin, H.; Zhou, C.; Tian, Y.; Siegrist, T.; Ma, B. Low-Dimensional Organometal Halide Perovskites. *ACS Energy Lett.* **2018**, *3*, 54–62.
- (18) Ghosh, S.; Kumar, J.; Nim, G. K.; Bag, M.; Kar, P. Air stable highly luminescent 2D tin halide perovskite nanocrystals as photodetectors. *Chem. Commun.* **2023**, *59*, 2110–2113.
- (19) Zhu, T.; Shen, L.; Xun, S.; Sarmiento, J. S.; Yang, Y.; Zheng, L.; Li, H.; Wang, H.; Bredas, J. L.; Gong, X. High-Performance Ternary Perovskite-Organic Solar Cells. *Adv. Mater.* **2022**, e2109348.
- (20) Mao, L.; Stoumpos, C. C.; Kanatzidis, M. G. Two-Dimensional Hybrid Halide Perovskites: Principles and Promises. *J. Am. Chem. Soc.* **2019**, *141*, 1171–1190.
- (21) Yao, Y.; Cao, D.; Yan, J.; Zhang, M.; Chen, X.; Shu, H. Spacer Cation Engineering of Two-Dimensional Hybrid Perovskites with Tunable Band Alignment and Optoelectronic Properties. *J. Phys. Chem. C* **2022**, *126*, 8408–8416.
- (22) Quan, L. N.; Yuan, M.; Comin, R.; Voznyy, O.; Beauregard, E. M.; Hoogland, S.; Buin, A.; Kirmani, A. R.; Zhao, K.; Amassian, A. et al. Ligand-Stabilized Reduced-Dimensionality Perovskites. *J. Am. Chem. Soc.* **2016**, *138*, 2649–55.
- (23) Tao, W.; Zhang, Y.; Zhu, H. Dynamic Exciton Polaron in Two-Dimensional Lead Halide Perovskites and Implications for Optoelectronic Applications. *Acc. Chem. Res.* **2022**, *55*, 345–353.
- (24) Kresse, G.; Hafner, J. Abinitio Molecular-Dynamics for Liquid-Metals. *Phys. Rev. B* **1993**, *47*, 558–561.

- (25) Kresse, G.; Furthmüller, J. Efficiency of ab-initio total energy calculations for metals and semiconductors using a plane-wave basis set. *Comput. Mater. Sci.* **1996**, *6*, 15–50.
- (26) Kresse, G.; Furthmüller, J. Efficient iterative schemes for ab initio total-energy calculations using a plane-wave basis set. *Phys. Rev. B* **1996**, *54*, 11169–11186.
- (27) Blöchl, P. E. Projector augmented-wave method. *Phys. Rev. B* **1994**, *50*, 17953–17979.
- (28) Perdew, J. P.; Burke, K.; Ernzerhof, M. Generalized gradient approximation made simple. *Phys. Rev. Lett.* **1996**, *77*, 3865.
- (29) Grimme, S.; Antony, J.; Ehrlich, S.; Krieg, H. A consistent and accurate ab initio parametrization of density functional dispersion correction (DFT-D) for the 94 elements H-Pu. *J. Chem. Phys.* **2010**, *132*, 154104.
- (30) Teter, M. P.; Payne, M. C.; Allan, D. C. Solution of Schrodinger’s equation for large systems. *Phys. Rev. B* **1989**, *40*, 12255–12263.
- (31) Bylander, D. M.; Kleinman, L.; Lee, S. Self-consistent calculations of the energy bands and bonding properties of B12C3. *Phys. Rev. B* **1990**, *42*, 1394–1403.
- (32) Heyd, J.; Scuseria, G. E. Efficient hybrid density functional calculations in solids: assessment of the Heyd-Scuseria-Ernzerhof screened Coulomb hybrid functional. *J. Chem. Phys.* **2004**, *121*, 1187–92.
- (33) Klein, G. J. M. M. L. Nosé–Hoover chains: The canonical ensemble via continuous dynamics. *J. Chem. Phys.* **1992**, *97*, 2635.
- (34) Taylor, J.; Guo, H.; Wang, J. Ab initio modeling of quantum transport properties of molecular electronic devices. *Phys. Rev. B* **2001**, *63*.
- (35) Perdew, J. P.; Zunger, A. SELF-INTERACTION CORRECTION TO DENSITY-FUNCTIONAL APPROXIMATIONS FOR MANY-ELECTRON SYSTEMS. *Phys. Rev. B* **1981**, *23*, 5048–5079.

- (36) Troullier, N.; Martins, J. L. EFFICIENT PSEUDOPOTENTIALS FOR PLANE-WAVE CALCULATIONS. *Phys. Rev. B* **1991**, *43*, 1993–2006.
- (37) Soler, J. M.; Artacho, E.; Gale, J. D.; Garcia, A.; Junquera, J.; Ordejon, P.; Sanchez-Portal, D. The SIESTA method for ab initio order-N materials simulation. *J. Phys.-Condes. Matter* **2002**, *14*, 2745–2779.
- (38) Lu, T.; Chen, F. Multiwfn: a multifunctional wavefunction analyzer. *J. Comput. Chem.* **2012**, *33*, 580–92.
- (39) Frisch, M. J.; Trucks, G. W.; Schlegel, H. B.; Scuseria, G. E.; Robb, M. A.; Cheeseman, J. R.; Scalmani, G.; Barone, V.; Mennucci, B.; Petersson, G. A. et al. Gaussian 09 Revision D.01. Gaussian Inc. Wallingford CT 2009.
- (40) Wu, T.; Wang, J. Deep Mining Stable and Nontoxic Hybrid Organic-Inorganic Perovskites for Photovoltaics via Progressive Machine Learning. *ACS Appl. Mater. Interfaces* **2020**, *12*, 57821–57831.
- (41) Park, I. H.; Zhang, Q.; Kwon, K. C.; Zhu, Z.; Yu, W.; Leng, K.; Giovanni, D.; Choi, H. S.; Abdelwahab, I.; Xu, Q. H. et al. Ferroelectricity and Rashba Effect in a Two-Dimensional Dion-Jacobson Hybrid Organic-Inorganic Perovskite. *J. Am. Chem. Soc.* **2019**, *141*, 15972–15976.
- (42) Kim, C.; Huan, T. D.; Krishnan, S.; Ramprasad, R. A hybrid organic-inorganic perovskite dataset. *Scientific Data* **2017**, *4*, 170057.
- (43) Wu, T.; Chen, X.; Wang, J. Metal-Free Hybrid Organic-Inorganic Perovskites for Photovoltaics. *J. Phys. Chem. Lett.* **2020**, *11*, 5938–5947.
- (44) Shockley, W.; Queisser, H. J. Detailed Balance Limit of Efficiency of p-n Junction Solar Cells. *J. Appl. Phys.* **1961**, *32*, 510.

- (45) Ma, L.; Dai, J.; Zeng, X. C. Two-Dimensional Single-Layer Organic-Inorganic Hybrid Perovskite Semiconductors. *Adv. Energy Mater.* **2017**, *7*, 1601731.
- (46) Wang, F.; Tan, M.; Li, C.; Niu, C.; Zhao, X. Unusual pressure-induced electronic structure evolution in organometal halide perovskite predicted from first-principles. *Org. Electron.* **2019**, *67*, 89–94.
- (47) Yu, P. Y.; Cardona, M. Fundamentals of Semiconductors: Physics and Materials Properties, 4th ed. *Springer, Berlin.* **2010**,
- (48) Frost, J. M.; Butler, K. T.; Brivio, F.; Hendon, C. H.; van Schilfgaarde, M.; Walsh, A. Atomistic origins of high-performance in hybrid halide perovskite solar cells. *Nano Lett.* **2014**, *14*, 2584–90.
- (49) Umari, P.; Mosconi, E.; De Angelis, F. Infrared Dielectric Screening Determines the Low Exciton Binding Energy of Metal-Halide Perovskites. *J. Phys. Chem. Lett.* **2018**, *9*, 620–627.
- (50) Filip, M. R.; Qiu, D. Y.; Del Ben, M.; Neaton, J. B. Screening of Excitons by Organic Cations in Quasi-Two-Dimensional Organic–Inorganic Lead-Halide Perovskites. *Nano Lett.* **2022**, *22*, 4870–4878.
- (51) Quan, J.; Yu, S.; Xing, B.; He, X.; Zhang, L. Two-dimensional Ruddlesden-Popper halide perovskite solar absorbers with short-chain interlayer spacers. *Phys. Rev. Mater.* **2022**, *6*, 065405.
- (52) Chen, X.; Wu, T.; Zhuang, W. Effectively modulating vertical tunneling transport by mechanically twisting bilayer graphene within the all-metallic architecture. *Nanoscale* **2020**, *12*, 8793–8800.
- (53) Datta, S. Electronic Transport in Mesoscopic System. *Cambridge University Press, Cambridge, England* **1995**,